Analyst

PAPER

View Article Online
View Journal | View Issue

Check for updates

Cite this: *Analyst*, 2021, **146**, 5610

Published on 19 July 2021. Downloaded by MIT Library on 2/9/2023 5:17:57 PM.

In situ detection of heavy metal ions in sewage with screen-printed electrode-based portable electrochemical sensors†

Qiwen Bao,[a] Gang Li,[a] Zhengchun Yang,[b] Peng Pan,[a] Jun Liu,[b] Ruirui Li,[b] Jun Wei,[c] Wei Hu,[d] Wenbo Cheng[e] and Ling Lin *[a]

The rapid development of industrial technologies continuously increases the heavy metal pollution of water resources. Recently, portable electrochemical analysis-based devices for detecting heavy metal ions have attracted much attention due to their excellent performance and low fabrication costs. However, it has proven difficult to accommodate complex testing needs in a cost-effective manner. To address these limitations, we propose a new system for the *in situ* detection of heavy metals in wastewater using an organic light-emitting diode-based panel to display data in real time and Bluetooth to transmit data to a smartphone for rapid analysis. The fabricated device integrates an *in situ* signal analysis circuit, a Bluetooth chip, a photocured 3D-printed shell, and an electrode sleeve interface. In addition, a fully screen-printed functional electrode plate containing chitosan/PANi–Bi nanoparticle@graphene oxide multi-walled carbon nanotubes is utilized for the rapid detection of heavy metal ions. This device can perform wireless data transmission and analysis and *in situ* signal acquisition and processing. The sensor exhibits a high sensitivity (Hg^{2+}: 88.34 μA ppm^{-1} cm^{-2}; Cu^{2+}: 0.956 μA ppm^{-1} cm^{-2}), low limit of detection (Hg^{2+}: 10 ppb, Cu^{2+}: 0.998 ppm) and high selectivity during the detection of copper and mercury ions in tap water under non-laboratory conditions, and the results of real-time tests reveal that parameters measured in the field and laboratory environments are identical. Hence, this small, portable, electrochemical sensor with a screen-printed electrode can be effectively used for the real-time detection of copper and mercury ions in complex water environments.

Received 8th June 2021,
Accepted 19th July 2021

DOI: 10.1039/d1an01012c

rsc.li/analyst

1. Introduction

Water is a non-renewable resource that is widely used in various human activities. However, industrial wastewater has become a major pollutant threatening human survival due to recent scientific and technological developments. The contents of toxic elements in industrial wastewater depend on the industrial plant type; there are acidic and alkaline wastewaters, wastewater containing organic phosphorus, radioactive wastewater, and wastewater containing heavy metal ions.[1] Among these contaminants, heavy metal ions are the most common and harmful toxic elements. Severe damage is caused by heavy-metal sewage because of the following reasons: (1) heavy-metal ions can be easily transported and thus accumulate in many levels of the food chain, which ultimately affects human beings the most because they are located at the top of the food chain. However, these ions cannot be eliminated by the body's natural metabolism, leading to chronic poisoning and the deterioration of human health.[2] (2) Even a small amount of heavy metal ions entering the human body may produce serious consequences. For example, a small amount of copper can lead to Alzheimer's disease. Copper poisoning also causes gastrointestinal problems, kidney damage, hair loss, nausea, anemia, hypoglycemia, and even death.[3] All forms of mercury, even trace amounts of it, are highly toxic to the human body due to their ease of accumulation.[4] Hence, the *in situ* detection of potential heavy metal contaminants in various water matrices is an important prerequisite for the

[a]*School of Precision Instrument and Optoelectronic Engineering, the State Key Laboratory of Precision Measuring Technology and Instruments, Tianjin University, 92 Weijin Road, Tianjin 300072, China. E-mail: linling@tju.edu.cn*
[b]*School of Electrical and Electronic Engineering, Tianjin Key Laboratory of Film Electronic & Communication Devices, Advanced Materials and Printed Electronics Center, Tianjin University of Technology, Tianjin 300384, China*
[c]*School of Materials Science and Engineering, Harbin Institute of Technology, Shenzhen 518055, China*
[d]*Tianjin Guokeyigong Science and Technology Development Co., Ltd, Tianjin 300399, China*
[e]*Suzhou Institute of Biomedical Engineering and Technology, Chinese Academy of Sciences Suzhou, 215163, P. R. China*
†Electronic supplementary information (ESI) available. See DOI: 10.1039/d1an01012c

This journal is © The Royal Society of Chemistry 2021

Published on 19 July 2021. Downloaded by MIT Library on 2/9/2023 5:17:57 PM.

removal and treatment of water pollutants. Atomic absorption spectroscopy,[5] inductively coupled plasma mass spectrometry,[6] X-ray fluorescence spectroscopy,[7] neutron activation analysis, inductively coupled plasma optical emission spectrometry,[8] and various optical methods (such as spectrophotometry)[9] have been successfully used in the detection and analysis of heavy metal ions. However, all these high-precision analytical techniques require expensive precision instruments, complex sample pretreatment procedures, and excellent instrument operation skills, making the field analysis process very complicated.[10] In contrast, electrochemical analysis is widely used due to its low cost and various other advantages, such as its high sensitivity, high selectivity, and low detection limit. Furthermore, it does not require electrodes with a specific surface area, which facilitates its integration and miniaturization.[11]

Powerful smartphones with integrated screen displays, data transfer and online analysis modules, advanced data processing capabilities, and open-source operating systems allow for further simplification of electronic designs and the miniaturization of circuit boards.[12] Meanwhile, an on-chip organic light-emitting diode (OLED) may be required for devices employing fast data acquisition when obtaining field test results or for unique situations wherein a mobile phone is not available or ran out of power. To satisfy the data transmission and power supply requirements of portable devices, many researchers focused on the use of mobile phone USB connections and audio interfaces, as well as portable device connections.[13] In particular, near-field communication (NFC) technology is widely applied to ensure the portability of electrochemical field analysis equipment and effective data transmission regardless of the power supply operation.[14] It is well known that the NFC efficiency strongly depends on the distance to the receiving terminal device, which usually does not exceed 5 cm.[15] For this reason, circuit design convenience is often sacrificed for a flexible communication distance. A system powered by Bluetooth and a tiny lithium-ion battery is more acceptable for long-distance communication while ensuring a long battery life. Bluetooth technology has a communication distance of 10–100 m and a very high data transmission rate. It is also compatible with smartphones and suitable for complex test environments, and satisfies real-time data transmission requirements.[16–18]

The majority of industrial electrode pattern manufacturing processes constitute top-down methods, such as wet chemical etching,[19] laser sintering,[20] stamp transfer,[21] and mask spraying.[22] These advanced techniques can be employed to produce high-precision electrodes. However, the cost of such electrodes is generally high, and the described methods are not suitable for mass electrode production (especially in the case of low-cost portable devices). Meanwhile, the availability of commercial substrates and printing equipment has made the screen-printing process applicable to small-scale, industrial electrode production. The majority of screen-printed electrodes contain ceramic and plastic substrates, and their costs are relatively low.[23] Among these substrates, polyethylene terephthalate (PET) possesses excellent folding and portability properties. Furthermore, in the field of trace heavy metal ion detection, bismuth film electrodes demonstrate high electrochemical performance during mercury detection and can effectively replace toxic mercury electrodes. Composite bismuth film electrodes modified with other functional materials, such as carbon paste electrodes coated with bismuth films[24] and chitosan/PANi–Bi nanoparticle@graphene oxide multi-walled carbon nanotubes (CS/PANi–Bi NP@GO–MWCNTs),[25] possess relatively high sensitivity and low detection limits for trace substance detection. Ultraviolet (UV) curing and three-dimensional (3D) printing technologies based on local light polymerization processes that utilize liquids containing a light initiator and polymer layers of the curing ink have many advantages. These include low manufacturing costs, the ability to easily produce complex shapes, and a printing precision in the micrometer range.[26] Furthermore, these properties are superior to the corresponding parameters of traditional fabrication methods, including fused deposition, spraying, selective laser sintering, direct writing, and stereolithography.

In this study, we combined Bluetooth technology, a miniature lithium-ion battery power module, an OLED module (used for online data display), and an inexpensive screen-printed electrode on a tiny circuit board for the high-performance detection of mercury and copper ions. In addition, UV-curing 3D printing technology was utilized to design and print a portable shell and electrode sleeve interface. An ultra-low power Bluetooth master chip ensured that the produced device maintained high performance and satisfied the requirements of flexible field testing. The active electrode contained Bi NP@GO–MWCNTs, which is a composite, functional material that was mentioned previously.[25] The obtained results showed that the fabricated electrode exhibited high sensitivity, repeatability, selectivity, and stability during the detection of heavy metal ions in tap water. The proposed, flexible heavy metal ion *in situ* detection technique based on the OLED-online or smartphone analyses can be potentially used in the development of a quality control procedure for complex industrial wastewater, marine water, and water matrices in other fields.

2. Experimental

2.1 Designing a portable heavy metal ion detection system

As shown in Fig. 1, the fabricated device is composed of a circuit board with an RF52832 main control chip, a thin sheet electrode, a 3D-printed component, and an electrode shell. A 77.50 × 66.30 × 1.6 mm FR-4 substrate circuit board (Fig. 1(a)) was incorporated into a miniature lithium-ion battery power supply module (Fig. 1(d)) together with a mode-selection module (Fig. 1(e)), a signal-transmission module (Fig. 1(f)), and a data display module (Fig. 1(g)). The PET-based screen-printed electrode can be used for field ion detection in two different modes, including that which employs a 3D printed microelectrolytic cell (Fig. 1(b)) and the real-time detection mode involving a drip-coating method (Fig. 1(c)).

A 1 × 1.2 mm, 5 mm thick 3D-printed electrode sleeve connector with a central opening was utilized for electrode mount-

Published on 19 July 2021. Downloaded by MIT Library on 2/9/2023 5:17:57 PM.

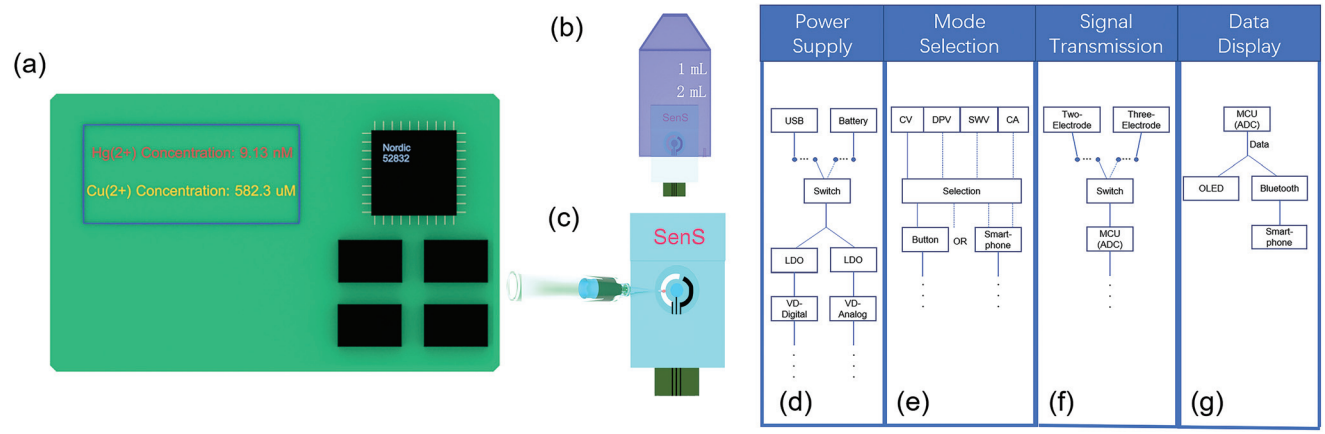

Fig. 1 Design and fabrication of a portable heavy-metal ion detection system equipped with a micro-battery and connected to an organic light-emitting diode (OLED) or a smartphone. (a) Top view. (b) Electrode connected to the 3D printed microelectrolytic cell. (c) Real-time detection using the dip coating method. Block diagrams of the (d) power supply module, (e) working mode selection module, (f) signal transmission module, and (g) data display module.

ing (Fig. 1(b) and (c)). To satisfy the field-testing requirements, a microelectrolytic cell was designed based on photocuring and 3D-printing technology and contained an opening in the upper part for the insertion of a syringe needle (Fig. 1(b)). Another testing method involved direct liquid dropping into the central opening of the electrode sleeve joint with a pipetting gun, which is similar to using a microelectrolytic cell with an opening to the surrounding space (Fig. 1(c)).

The block diagram of the power supply module of the entire device is shown in Fig. 1(d). First, it selects between the battery power and USB power with a double-ended toggle switch. After that, the power is supplied to the digital voltage circuit and analog voltage circuit through a two-path regulated voltage output circuit (MIC520, Micrel). The block diagram of the operating mode selection module is shown in Fig. 1(e). It utilizes a signal switch (MAX4644EUT, Maxim) to choose between the voltage and current modes and then sets the digital-to-analog converter (DAC) and timing cycle for different testing methods, such as cyclic voltammetry (CV), differential pulse voltammetry (DPV), square wave voltammetry (SWV), and chronoamperometry (CA), using smartphone virtual buttons.

Fig. 1(f) displays the block diagram of the signal transmission module. It uses a signal switch (MAX4643EUA, Maxim) to select between the two-electrode and three-electrode working modes. The measured potential or current signal is transmitted to the built-in analog-to-digital converter (ADC) of the microcontroller (MCU; NRF52832, Nordic) through an integrated operational amplifier (AD8608ARUZ, ADI). Finally, Fig. 1(g) shows the dual-terminal data display module. Using this module, the digital signals converted by ADC can be displayed in real time on a 3.2 cm OLED and transmitted to smartphones by the Bluetooth function of the MCU *via* an on-chip antenna. An app on the phone sends commands to the device *via* Bluetooth to select a desired electrode system (two-electrode or three-electrode) and operating mode; it can also receive data for visual display. The various commercial chip models used in the ion detection equipment and their unit prices are listed in Table 1. It shows that the portable system designed in this study for the field analysis of heavy metal ions has distinct cost advantages.

2.2 Chemical modifications of the electrode for detecting Hg^{2+} and Cu^{2+} ions

As illustrated in Fig. 2(e), the CS/PANi–Bi NP@GO–MWCNT screen-printed carbon electrode (SPCE) was prepared *via* layer-by-layer printing and dispensing. First, the following steps were performed to synthesize the PANi–Bi NP@GO–MWCNT ink: (1) MWCNTs (30 mg) were added to a beaker containing 10 mL of an aqueous graphene solution (1 mg mL^{-1}). The resulting system was stirred and then placed in an ultrasonic bath at 5–35 °C for 2 h. (2) A high-speed centrifuge was utilized to successively separate the obtained solution at 8000 and 12 000 rpm s^{-1}. The produced black powder was extracted and filtered for use in the lower layer of a centrifuge tube. (3) The

Table 1 Unit prices of various ion detection devices and their components

Components	Cost ($)	Components	Cost ($)
GH7540CT-ND (TOGGLELARGE)	4.7	3.7 V lithium-ion battery	1
CP-032HPJCT-ND (DC_JACK_0.7MM)	0.8	CP-032HPJCT-ND (DC_JACK_0.7MM)	0.8
576-1259-1-ND (LDO-MIC5205-3.3YM5-TR)	0.72	576-1259-1-ND (LDO-MIC5205-3.3YM5-TR)	0.36
AD5667RBRMZ-2-ND	9.08	Resistance and capacitance	0.059
AD8608ARUZ	4	PCB	0.5
MAX4643EUA+	1.2	3D printing module	0.78
MAX4644EUT + T	2.37	OLED	1.31
MK-02A (nRF-52832)	3	Connection terminals	0.05
Cost ($)	30.73		

This journal is © The Royal Society of Chemistry 2021

Published on 19 July 2021. Downloaded by MIT Library on 2/9/2023 5:17:57 PM.

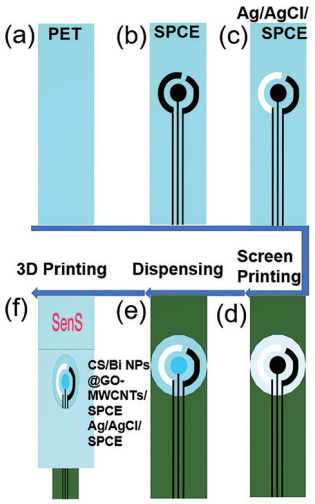

Fig. 2 Electrode fabrication and modification processes. (a) Polyethylene terephthalate (PET) substrate. (b) Screen-printed pure carbon patterns and wires. (c) Screen-printed Ag/AgCl films for the reference electrode. (d) Screen-printed isolation layers. (e) Chitosan/PANi–Bi nanoparticle@graphene oxide multi-walled carbon nanotube (CS/PANi–Bi NP@GO–MWCNT) film deposited on the working electrode with a dispenser. (f) 3D printed electrode sleeve connector.

obtained black GO–MWCNT powder was mixed with 230 mg of bismuth nitrate powder and 50 mL of dimethylformamide (1 mg mL^{-1}) and then dispersed by ultrasonic treatment for 30 min. (4) Hydrazine (0.87 mL) was then added to the reaction mixture, which was subsequently refluxed at 160 °C. After 3 h, the remaining black powder was removed and cleaned. (5) The PANi–Bi NP@GO–MWCNT ink was obtained by mixing 10 g of the previously prepared PANi reagent[27] and all the obtained black powder and then dispersing the mixture in an ultrasonic bath for 30 min. The preparation of a polyvinyl acetate thickener and the CS protective film was conducted according to a previously reported procedure.[25] Finally, the obtained PANi–Bi NPs@GO–MWCNTs were mixed with the thickener at a 20 wt% filling ratio.

As shown in Fig. 2(b)–(d), an automatic flat screen-printing machine (WY-4060, Langfang Screen Printing Fest Screen Printing Materials Co., Ltd, China) was used to fabricate a pure carbon substrate pattern, a wire layer, a reference electrode containing an Ag/AgCl film, and an isolation layer by layer-to-layer printing. A dispenser (SM200SX-3A, Musashi, Japan) was utilized to uniformly draw a solid circle pattern with a diameter of 1 cm at the center of the working electrode (Fig. 2(e)). Finally, a UV-curing 3D printer (Slash Plus, UNIZ, China) was employed to print a card sleeve structure with a central opening for the electrode plate, which resembled a microelectrolytic cell.

Specially customized 200-mesh plates were applied as substrates for printing a half moon-type reference electrode and an insulation layer with a hole in the central area. The PET surface was successively cleaned with anhydrous ethanol and deionized water and then placed in a dry air dryer at 80 °C for 30 min (Fig. 2(b)). Commercial, pure carbon ink (Shenzhen Jieyong Technology Co., Ltd, China) was used to print a uniform pattern layer on the PET surface, which was then placed in the dryer at 120 °C for 30 min. Next, commercial, pure silver ink (Shanghai Russell Technology Co., Ltd, China) was utilized to print the silver film reference electrode on the cleaned and dried SPCE (Fig. 2(c)). The obtained Ag electrode was immersed in a 5 M iron bromide solution for 1 min and then dried in a drying oven at 60 °C for 30 min to produce an Ag/AgCl electrode. In the next step, a layer of commercial, insulating oil (Shenzhen Jieyong Technology Co., Ltd, China) was applied to the electrode surface (excluding the working electrode, reference electrode, and counter electrode areas) and then placed in a dryer at 120 °C for 30 min (Fig. 2(d)). The dispenser was used to absorb 1 mL of the aforementioned composite modification material, and the prepared PANi–Bi NP@GO–MWCNTs were employed to draw a circular pattern in the central working electrode area at 15.9 kW. After that, both the needle and needle tube were replaced to absorb 1 mL of the CS solution and draw a CS ion protective film at 9.8 kW. Finally, a small card sleeve for the electrode sheet was fabricated using UV curing 3D printing technology for the sake of esthetics and practicability.

2.3 Qualitative characterization

Fig. 3(a and c) show the morphology and regional element distribution of the PANi–Bi NP@GO–MWCNTs at a magnification of 8000×. The first image clearly shows that the GO–MWCNTs grown on the surface of the PANi-modified SPCE are microporous with well-interconnected networks. In combination with Fig. 3(c), we find that in the three-dimensional framework of PANi@GO–MWCNTS, Bi nanoparticles are immobilized in the three-dimensional network through the electrostatic interaction between particles.

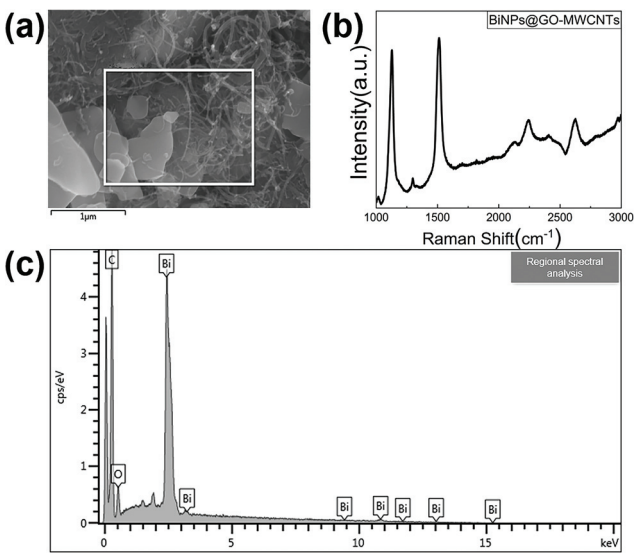

Fig. 3 Ultrahigh-resolution SEM (a) and EDX spectra (c) of PANi–Bi NP@GO–MWCNTs; the Raman spectra of PANi–Bi NP@GO–MWCNTs (b).

Published on 19 July 2021. Downloaded by MIT Library on 2/9/2023 5:17:57 PM.

The Raman spectra of PANi–Bi NP@GO–MWCNTs are shown in Fig. 3(b). The three characteristic peaks at 1128 cm^{-1}, 1512 cm^{-1} and 2625 cm^{-1} of PANi–Bi NP@GO–MWCNTs correspond to the typical D, G and 2D bands of GO–MWCNTs.[28] The characteristic peak at 1298 cm^{-1} may be related to Bi–O formed by the oxidation of Bi nanoparticles in a hot water bath compared with the data from the previous work.[29] Thus, the Raman data further confirmed the successful preparation of the PANi–Bi NP@GO–MWCNT composite.

2.4 UV printing of the device cover and electrode sleeve connectors

A compact and efficient desktop photocuring printer with an 8.9-inch 4K high-definition liquid crystal display-based optical engine was used for the fabrication of the device cover and electrode sleeve connectors. Its printing accuracy was approximately 10 μm, which enabled a high-performance detailed printing process. The printer tank was filled with Zabs Gray resin supplied by Uniz, which was characterized by a high curing speed, strong surface adhesion, acrylonitrile butadiene styrene (ABS)-like performance, low odor, high storage resistance, and high versatility. The printed model had a relatively smooth surface and the following design and printing parameters: a 92.52 × 81.5 × 10.2 mm shell with a special opening and a sleeve joint with dimensions of 2 × 2 cm containing a round hole with a diameter of 1 cm at the center of the upper surface designed using Rhino 7 software according to the functional requirements and sizes of the circuit board and electrode sheet. Subsequently, an STL file was generated for the subsequent production processes. By importing this file into the supporting production software of the machine, automatic printing was performed while pouring a necessary amount of the resin. After approximately 30 min, the model was removed and polished with a hand-held grinder to smooth its surface. The final picture of the finished product is shown in Fig. S1 (ESI).†

2.5 Evaluation of Hg^{2+} and Cu^{2+} sensors

In previous studies,[25,27] a commercial phosphate-buffered saline solution with a fixed pH was used for testing purposes. Herein, the buffer solution was replaced with untreated tap water in this work to satisfy the on-site testing requirements. The concentrations of heavy metal ions detected in the analyzed water were significantly lower than the maximum amounts allowed in drinking water for it to be deemed safe by the World Health Organization (WHO) and the Environmental Protection Agency (EPA) (see Table 2). The following steps were performed during testing: First, mercury ion standard solution was used to prepare 2, 4, 6, 10, 14, 20, 40, 60, 80, 100, 120, 140 160 and 180 ppb mercury-ion solutions. After that, a 120 ppb mercury-ion solution was obtained as an unknown control group. Similarly, copper ion standard solutions (0.998, 1.495, 1.992, 2.487, 3.457, 3.968, 4.459, 4.95, 5.928, 6.903, 7.874, 9.803, 12.195, 14.563 and r16.908 ppm) were prepared as the experimental group, and a 2.982 ppm mercury ion standard solution was prepared as the unknown control group.

Table 2 Standards and guidelines developed for the concentrations of heavy metals in drinking water by the World Health Organization (WHO) and the Environmental Protection Agency (EPA)

Metal	WHO (mg L^{-1})	EPA (mg L^{-1})
Hg	0.01	0.01
Cu	2	1.3
Pb	0.01	0.015
Cd	0.003	0.005
Zn	3	5
As	0.01	0.01
Ni	0.07	0.04

The electrode was connected to the miniature workstation, as shown in Fig S2.† At the same time, a mini lithium-ion battery was used as the power supply to test the portability and reflect real-time field testing conditions. Commands and data were transmitted through the built-in Bluetooth interface. Instructions were inputted to the micro-workstation through a mobile phone app to set the modes of the system, namely the three-electrode system and the DPV method.

The outer part of the electrode sheet was sheathed with an electrolytic cell electrode sleeve joint, which was designed and manufactured using a light-curing 3D printer. This sleeve not only immobilized the electrode sheet and protected it from stress, but also created a semi-closed cylindrical space between the three-electrode region and the external environment. The analyzed solution could be added and removed only through the upper space region.

The testing procedure was divided into two successive parts. For mercury ion detection, 1 mL of the solution was added dropwise into the cylindrical working area using a 100–1000 μL pipetting gun. After that, DPV data were obtained at a specified concentration of mercury ions. In the next step, the electrode surface was gently cleaned with tap water and air-dried at room temperature for 5 min. The concentration of mercury ions was then determined. The unknown control group was tested after examining all samples in the experimental group (before this step, the OLED was set to display the mercury ion concentration in the unknown solution in real time through Bluetooth). Finally, a control experiment was performed using the cylindrical working electrode, and the produced data were transmitted *via* the OLED and Bluetooth.

The copper-ion testing procedure conducted for the second group of samples was similar to that described in the previous paragraph. The data received *via* Bluetooth were further analyzed to evaluate the performance of the micro-workstation and the suitability of the electrode for heavy metal ion detection.

3 Results and discussion

3.1 Characterization of the Hg^{2+} sensor

The DPV plots based on the mercury-ion measurement data transmitted through the Bluetooth module of the micro-workstation are shown in Fig. 4. Fig. 4(a) depicts the current density (A cm^{-2})–potential (V) curves of the CS/PANi–Bi

 This journal is © The Royal Society of Chemistry 2021

Published on 19 July 2021. Downloaded by MIT Library on 2/9/2023 5:17:57 PM.

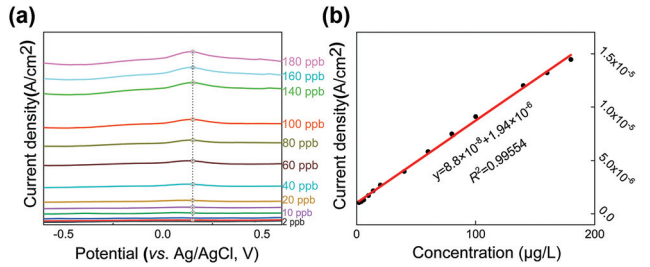

Fig. 4 (a) Differential pulse voltammetry (DPV) curves recorded using the CS/PANi–Bi NP@GO–MWCNT screen-printed carbon electrode (SPCE) in tap water containing 10–200 μg L^{-1} Hg^{2+} ions. (b) Linear fitting curve obtained for the data presented in panel (a).

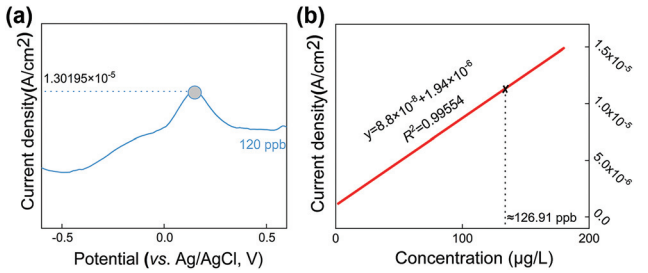

Fig. 5 DPV data and results of the control experiment. (a) DPV curve recorded using the CS/PANi–Bi NP@GO–MWCNT SPCE in tap water containing 120 ppb of Hg^{2+} ions. (b) Comparison of the measured Hg^{2+} concentration with the nominal value.

NP@GO–MWCNT electrode obtained upon the analysis of tap water solutions containing 10–200 ppb of Hg^{2+} ions. The voltage window was −0.6 V to +0.6 V, and the scan rate was 50 mV s^{-1}. These results show a peak of the increasing current intensity at approximately +0.148 V and a shift in the positive voltage direction observed in the aqueous environment. The linear fitting curve obtained for the data presented in Fig. 4(a) is shown in Fig. 4(b), which confirms that the prepared electrode exhibits good linearity (R^2 = 0.99554), high sensitivity (88.34 μA ppm^{-1} cm^{-2}), and a low limit of detection (LOD = 10 ppb) for Hg^{2+} ions. The CS/PANi–Bi NP@GO–MWCNT/SPCE yielded high peak currents, which is due to the three-dimensional framework of PANi@GO–MWCNTs anchored with Bi NPs, providing an increased surface and facilitating a better deposition for mercury ions. Also, the GO, MWCNTs, and PANi spread on the electrode surface increased the signal.[6] The improvement can be attributed to the high ionic conductivity and ion exchange properties of the polymer and GO–MWCNTs as well as to the surface area increase and electric conductivity of Bi NPs. The DPV curves clearly demonstrate that the bismuth film in combination with the PANi/GO/MWCNT composite possesses very attractive electrochemical characteristics.

A control experiment was also performed to evaluate the effectiveness of the micro-workstation and the electrochemical performance of the CS/PANi–Bi NP@GO–MWCNT electrode. First, the parameters of the linear fitting curve were determined and inputted into the program. The internal algorithm calculated the required values and displayed them on the OLED. The data transmitted to the computer *via* Bluetooth and the related statistics are shown in Fig. 5.

The current density (A cm^{-2})–potential (V) plot of the CS/PANi–Bi NP@GO–MWCNT electrode obtained in the 120 ppb Hg^{2+} ion solution is presented in Fig. 5(a). The current density near +0.148 V was used to determine the corresponding value in the linear fitting curve depicted in Fig. 5(b). We found that the measured value was approximately 126.91 ppb, which was close to the actual Hg^{2+} concentration of 120 ppb. The designed micro-electrochemical workstation and CS/PANi–Bi NP@GO–MWCNT electrode exhibited relatively high stability and good electrochemical performance considering the errors introduced by the device and solution preparation process.

3.2 Characterization of the Cu^{2+} sensor

Fig. 6(a) shows the current density (A cm^{-2})–potential (V) plots obtained for the fabricated device and CS/PANi–Bi NP@GO–MWCNT electrode during the detection of 0.5–16.908 ppm of Cu^{2+} ions in tap water. All curves contain the same, distinct, characteristic peaks centered at approximately −0.244 V. Fig. 6(b) depicts the linear fitting curve obtained in Fig. 6(a). We found that the current intensity at the characteristic peak near the potential = −0.244 V decreased with the increase of the concentration of copper ions. The reason why this happens is shown through the following deduction.

The conductivity formula of the electrolyte is as follows:

$$L = (A/l)e_0(n^+z^+u^+ + n^-z^-u^-) \quad (1)$$

where L is the conductance of the electrolyte solution, A is the electrode area, l is the distance between two electrodes, e_0 = 1.60218×10^{-19} C, n^+ and n^- are the ion concentrations, z^+ and z^- are the ion charges, and u^+ and u^- are the ion mobilities. The conductivity of an electrolyte is defined as the conductivity of an electrolyte solution per cubic centimeter volume. For an electrolytic cell with a uniform cross-sectional area (A), the distance between the two electrodes inserted into the solution is l, and the relationship between the conductivity (κ) and the conductivity (L) of the electrolyte solution is as follows:

$$\kappa = e_0(n^+z^+u^+ + n^-z^-u^-) \quad (2)$$

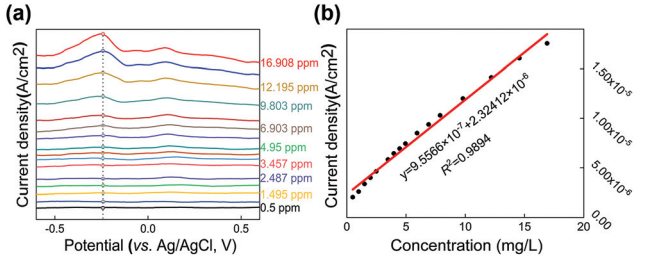

Fig. 6 (a) DPV curves recorded using the CS/PANi–Bi NP@GO–MWCNT SPCE in tap water containing 0.5–16.908 ppm of Cu^{2+} ions. Linear fitting curves obtained for (b).

Published on 19 July 2021. Downloaded by MIT Library on 2/9/2023 5:17:57 PM.

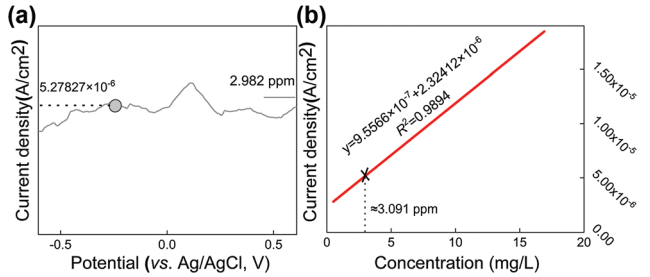

Fig. 7 DPV data and results of the control experiment. (a) DPV curves recorded using the CS/PANi–Bi NP@GO–MWCNT SPCE in tap water containing 2.982 ppm Cu^{2+} ions. (b) Comparison of the measured Cu^{2+} concentration with the nominal value.

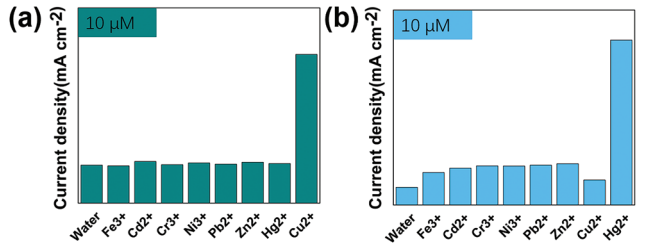

Fig. 8 Detected results of the comparison of the CS/PANi–Bi NP@GO–MWCNT electrode in tap water solution containing 10 μm Fe^{3+}, Cd^{2+}, Cr^{3+}, Ni^{3+}, Pb^{2+}, Zn^{2+}, Hg^{2+}, and Cu^{2+}, respectively: (a) potential = +0.148 V; (b) potential = −0.244 V.

According to eqn (2), the conductivity of the strong electrolyte has a linear relationship with the electrolyte concentration, but this linear relationship only holds for dilute solution systems. With the increase of the concentration of electrolyte solution, the distance between ions becomes smaller and the electrostatic interaction between ions increases rapidly. For highly concentrated electrolyte solutions, the Coulomb interaction between positive and negative ions causes ions to associate and form neutral particles, which do not contribute to the conductivity of the solution.

Therefore, this explains the phenomenon that the current intensity in Figs. 4 and 6 decreases with the increase of electrolyte concentration and the fitting curve of the electrode in Fig. 6 gradually deviates from the linear relationship in the presence of a high concentration of copper ions. This shows that the fabricated electrode exhibited good linearity (R^2 = 0.9894), high sensitivity (0.956 μA ppm^{-1} cm^{-2}), and a low LOD (0.5 ppm) for Cu^{2+} detection.

Meanwhile, the DPV curve recorded for the CS/PANi–Bi NP@GO–MWCNT electrode for the control group is shown in Fig. 7(a), while the linear fitting curve obtained at high Cu^{2+} concentrations is presented in Fig. 7(b). Here, the characteristic peak is located near −0.244 V and the measured Cu^{2+} content (3.091 ppm) is close to the actual value (2.982 ppm).

3.3 Stability of the CS/PANi–Bi NP@GO–MWCNT electrode

The fabricated CS/PANi–Bi NP@GO–MWCNT electrode maintained good reproducibility and electrochemical performance after multiple cleaning cycles and long testing and waiting times. Hence, the constructed micro-electrochemical workstation with the specified electrode exhibited high environmental and long-term stabilities.

3.4 Selectivity of the CS/PANi–Bi NP@GO–MWCNT electrode

The electrochemical performance of the CS/PANi–Bi NP@GO–MWCNT electrode was also tested in a solution containing other heavy metal ions. The obtained results presented in Fig. 8 revealed that the studied electrode showed good selectivity for Hg^{2+} and Cu^{2+} detection in tap water solution containing 10 μM Fe^{3+}, Cd^{2+}, Cr^{3+}, Ni^{3+}, Pb^{2+}, Zn^{2+}, Hg^{2+}, Cu^{2+}, respectively. The data presented in Fig. 4 and 6 show that both mercury and copper ions present in a complex water environment can be distinguished from one another by their characteristic peaks centered at different potentials. Therefore, the microelectrochemical workstation with the CS/PANi–Bi NP@GO–MWCNT electrode possesses high selectivity.

Table 3 Comparative parameters of the device fabricated in this work and widely used electrochemical workstations

	This work	Interface 1010B	Versa STAT 4	CompactStat	PalmSens
Techniques	POT, CA, CV, DPV, SWV	POT, CA, CV, DPV, SWV	POT, CA, CV, DPV, SWV, OCPT, CPI, LSV	POT, CA, CV, DPV, SWV, LSV, EIS	CA, CV, DPV, SWV, LSV, CC, ZRA, LSP
Voltage range	±1.5 V (67 μV resolution) 40 μV noise	±12 V (1 μV resolution) ± 0.3% of reading ± 1 mV	±10 V (6 μV resolution) ± 0.2% of reading ± 2 mV	±10 V (0.4 μV resolution) 16/40 nV	±10 V (76.3 μV resolution) ≤ 0.1% ± 1 mV offset
Current range	1 range: ±180 μA (6.4 nA resolution) 30 nA noise	9 range: ±1 A (1.5 pA resolution) ± 0.2% of reading, ±0.2% of range 4 nA: <0.5% ± 20 pA	10 range: ±2 A (120 fA resolution) ± 5 pA ± 0.3%	6 range: ±10 A (1.5 pA resolution) 0.15 fA	9 range: ±10 mA (5 fA resolution) ≤ 0.1% (in the full scale range)
Power source	Rechargeable battery	AC power	AC power	USB	Rechargeable battery
Connectivity to mobile phones	Wireless connection *via* Bluetooth low energy	NA	NA	WIFI	Wireless connection *via* Bluetooth
Cost ($)	30.73	38 650	61 880	23 205	9282

This journal is © The Royal Society of Chemistry 2021

Published on 19 July 2021. Downloaded by MIT Library on 2/9/2023 5:17:57 PM.

3.5 Cost advantage of the portable electrochemical workstation

Table 3 presents a comparison of the costs and characteristics of several popular desktop and portable electrochemical workstations with the corresponding parameters of the portable workstation designed in this study. It shows that low cost is a major advantage of the fabricated system, which provides sufficiently high measurement accuracy and resolution (notably, it weighs only 166 g and costs only $30). Furthermore, the use of a signal transceiver in the internal circuit and external DAC with high precision allowed for the configuration of several main electrochemical measurement methods, including CA, CV, DPV, and SWV, as well as two-electrode and three-electrode systems.

In recent years, an increasing number of researchers have attempted to develop portable and wearable devices for heavy metal ion detection. However, many of these products were purchased from other companies. The relatively high cost, complex fabrication process, and strict requirements for the electrode performance and preparation technology were the negative factors that impeded their development.[30,31] Meanwhile, the size of the circuit board manufactured in this work can be further reduced by optimizing its current version. In addition, a more portable electrochemical platform could be obtained in future studies by implementing NFC data transmission, wireless power supply technology, and a flexible circuit board design.

4 Conclusions

In this study, we developed a portable electrochemical mini workstation for the quantitative determination of Hg^{2+} and Cu^{2+} ion concentrations in tap water. The utilized electrode was first prepared by an economical and effective screen-printing process and then combined with a small electrochemical analytic device, a rapid signal acquisition system, and a transmission module. The concentrations of Hg^{2+} and Cu^{2+} ions were monitored in real time using a small OLED. The obtained results revealed that the produced sensor exhibited a high sensitivity (Hg^{2+}: 88.34 μA ppm^{-1} cm^{-2}; Cu^{2+}: 0.956 μA ppm^{-1} cm^{-2}) and a lowlimit of detection (Hg^{2+}: 10 ppb, Cu^{2+}: 0.998 ppm). Moreover, our evaluations of the tap water composition and the results of previous work conducted under laboratory conditions show a good correlation, indicating that our device provides a performance comparable to that of a commercial precision instrument. The proposed platform provides a new solution for the development of smartphone-based devices for the field detection of heavy metal ions in aquatic environments. Furthermore, our methodology could be used to significantly increase the flexibility and miniaturization degrees of similar testing systems. In the future, the manufactured electrode can be potentially used for the rapid detection of Hg^{2+} and Cu^{2+} ions in tap water, lake water, industrial wastewater, and other aqueous environments.

Author contributions

Qiwen Bao wrote the paper, performed the experiments, and designed the device; Gang Li supervised this work; Zhengchun Yang, Peng Pan, and Jun Liu guided the experiments; Jun Wei developed the methodology; and Wei Hu and Wenbo Cheng provided the experimental site and equipment. All authors contributed to the general discussion.

Conflicts of interest

The authors declare that they have no conflict of interest.

Acknowledgements

The authors would like to thank the State Key Laboratory of Precision Measuring Technology and Instruments for the use of their equipment. They are also thankful to Prof. Yang and Prof. Pan from Tianjin University of Technology for their guidance regarding experimental ideas and techniques as well as to Tianjin Guokeyigong Science and Technology Development Company for providing the access to the laboratory site and required equipment.

References

1 A. Kumar, P. Raizada, P. Singh, R. V. Saini, A. K. Saini and A. Hosseini-Bandegharaei, *Chem. Eng. J.*, 2020, **391**, 123496.
2 M. A. Al-Ghouti, J. Li, Y. Salamh, N. Al-Laqtah, G. Walker and M. N. M. Ahmad, *J. Hazard. Mater.*, 2010, **176**, 510–520.
3 G. J. Brewer, *J. Am. Coll. Nutr.*, 2009, **28**, 238–242.
4 O. Caylak, S. G. Elci, A. Hol, A. Akdogan, U. Divrikli and L. Elci, *Food Chem.*, 2019, **274**, 487–493.
5 T. Alizadeh and S. Amjadi, *J. Hazard. Mater.*, 2011, **190**, 451–459.
6 S. Chaiyo, E. Mehmeti, K. Zagar, W. Siangproh, O. Chailapakul and K. Kalcher, *Anal. Chim. Acta*, 2016, **918**, 26–34.
7 S.-M. Choi, D.-M. Kim, O.-S. Jung and Y.-B. Shim, *Anal. Chim. Acta*, 2015, **892**, 77–84.
8 C. Combellas, F. Kanoufi, J. Pinson and F. I. Podvorica, *J. Am. Chem. Soc.*, 2008, **130**, 8576–8577.
9 G. Aragay, J. Pons and A. Merkoci, *Chem. Rev.*, 2011, **111**, 3433–3458.
10 B. Bansod, T. Kumar, R. Thakur, S. Rana and I. Singh, *Biosens. Bioelectron.*, 2017, **94**, 443–455.
11 A. Duzgun, G. A. Zelada-Guillen, G. A. Crespo, S. Macho, J. Riu and F. X. Rius, *Anal. Bioanal. Chem.*, 2011, **399**, 171–181.
12 D. M. Zhang and Q. J. Liu, *Biosens. Bioelectron.*, 2016, **75**, 273–284.

Published on 19 July 2021. Downloaded by MIT Library on 2/9/2023 5:17:57 PM.

13 S. Li, J. L. Liu, Z. T. Chen, Y. L. Lu, S. S. Low, L. H. Zhu, C. Cheng, Y. He, Q. M. Chen, B. Su and Q. J. Liu, *Sens. Actuators, B*, 2019, **297**, 126811.
14 G. Xu, C. Cheng, W. Yuan, Z. Y. Liu, L. H. Zhu, X. T. Li, Y. L. Lu, Z. T. Chen, J. L. Liu, Z. Cui, J. J. Liu, H. Men and Q. J. Liu, *Sens. Actuators, B*, 2019, **297**, 126743.
15 P. Kassal, M. D. Steinberg and I. M. Steinberg, *Sens. Actuators, B*, 2018, **266**, 228–245.
16 E. Ghafar-Zadeh, *Sensors*, 2015, **15**, 3236–3261.
17 C. Chen, F. Tsow, K. D. Campbell, R. Iglesias, E. Forzani and N. J. Tao, *IEEE Sens. J.*, 2013, **13**, 1748–1755.
18 J. Kim, S. Imani, W. R. de Araujo, J. Warchall, G. Valdes-Ramirez, T. Paixao, P. P. Mercier and J. Wang, *Biosens. Bioelectron.*, 2015, **74**, 1061–1068.
19 Y. Y. Xia, J. Si and Z. Y. Li, *Biosens. Bioelectron.*, 2016, **77**, 774–789.
20 Z. L. Huang, Y. F. Hao, Y. Li, H. J. Hu, C. H. Wang, A. Nomoto, T. S. Pan, Y. Gu, Y. M. Chen, T. J. Zhang, W. X. Li, Y. S. Lei, N. Kim, C. F. Wang, L. Zhang, J. W. Ward, A. Maralani, X. S. Li, M. F. Durstock, A. Pisano, Y. Lin and S. Xu, *Nat. Electron.*, 2018, **1**, 473–480.
21 S. Li, B. N. Peele, C. M. Larson, H. C. Zhao and R. F. Shepherd, *Adv. Mater.*, 2016, **28**, 9770–9775.
22 L. H. Li, Y. Y. Bai, L. L. Li, S. Q. Wang and T. Zhang, *Adv. Mater.*, 2017, **29**, 1702517.
23 E. Bernalte, C. Marin Sanchez and E. Pinilla Gil, *Anal. Chim. Acta*, 2011, **689**, 60–64.
24 E. A. Hutton, S. B. Hocevar, B. Ogorevc and M. R. Smyth, *Electrochem. Commun.*, 2003, **5**, 765–769.
25 Q. Bao, G. Li, Z. Yang, P. Pan, J. Liu, J. Chang, J. Wei and L. Lin, *Chin. Chem. Lett.*, 2020, **31**, 2752–2756.
26 D. K. Patel, A. H. Sakhaei, M. Layani, B. Zhang, Q. Ge and S. Magdassi, *Adv. Mater.*, 2017, **29**, 1606000.
27 Q. W. Bao, Z. C. Yang, Y. F. Song, M. Y. Fan, P. Pan, J. Liu, Z. Y. Liao and J. Wei, *J. Mater. Sci.: Mater. Electron.*, 2019, **30**, 1751–1759.
28 T. Kokab, A. Shah, F. J. Iftikhar, J. Nisar, M. S. Akhter and S. B. Khan, *ACS Omega*, 2019, **4**, 22057–22068.
29 Q. W. Bao, G. Li, Z. C. Yang, P. Pan, J. Liu, J. Y. Chang, J. Wei and L. Lin, *Chin. Chem. Lett.*, 2020, **31**, 2752–2756.
30 M. Badea, F. di Modugno, L. Floroian, D. M. Tit, P. Restani, S. Bungau, C. Iovan, G. E. Badea and L. Aleya, *Sci. Total Environ.*, 2019, **672**, 129–140.
31 E. D. Yenilmez, U. Kokbas, K. Kartlasmis, L. Kayrin and A. Tuli, *PLoS One*, 2018, **13**, e0197855.

This journal is © The Royal Society of Chemistry 2021